# The phosphatase inhibitor Sds23 regulates cell division symmetry in fission yeast

Katherine L. Schutt and James B. Moseley*

Department of Biochemistry and Cell Biology
The Geisel School of Medicine at Dartmouth, Hanover, NH 03755

* Corresponding author
james.b.moseley@dartmouth.edu

**Running Title:** Sds23 regulates division symmetry in fission yeast

**Character count:** 19,816

## Abstract

Animal and fungal cells divide through the assembly, anchoring, and constriction of a contractile actomyosin ring (CAR) during cytokinesis. The timing and position of the CAR must be tightly controlled to prevent defects in cell division, but many of the underlying signaling events remain unknown. The conserved heterotrimeric protein phosphatase PP2A controls the timing of events in mitosis, and upstream pathways including Greatwall-Ensa regulate PP2A activity. A role for PP2A in CAR regulation has been less clear, although loss of PP2A in yeast causes defects in cytokinesis. Here, we report that Sds23, an inhibitor of PP2A family protein phosphatases, promotes the symmetric division of fission yeast cells through spatial control of cytokinesis. We found that *sds23*Δ cells divide asymmetrically due to misplaced CAR assembly, followed by sliding of the CAR away from its assembly site. These mutant cells exhibit delayed recruitment of putative CAR anchoring proteins including the glucan synthase Bgs1. Our observations likely reflect a broader role for regulation of PP2A in cell polarity and cytokinesis because *sds23*Δ phenotypes were exacerbated when combined with mutations in the fission yeast Ensa homolog, Igo1. These results identify the PP2A regulatory network as a critical component in the signaling pathways coordinating cytokinesis.

## Introduction

Organisms from yeast to humans build a contractile actomyosin ring (CAR) that drives cytokinesis. The fission yeast CAR assembles from a series of 50-75 precursor structures termed "nodes" in the plasma membrane (Chang et al., 1996; Sohrmann et al., 1996; Wu et al., 2006; Almonacid et al., 2009, 2011). Similar precursors have been observed in animal cell CAR assembly (Piekny and Glotzer, 2008). Nodes contain actin- and myosin-regulatory proteins, as well as membrane-binding proteins with the capacity to tether the CAR to the cell cortex (Wu *et al.*, 2006). During mitosis, nodes coalesce into an intact CAR. Past studies have defined the recruitment timing, functional contribution, and spatial organization of CAR proteins in fission yeast (Pollard and Wu, 2010; Laplante et al., 2016; McDonald et al., 2017). However, many

questions remain open regarding the upstream signaling pathways that ensure assembly of this complex structure at the correct time and place.

Fission yeast cells proceed through cytokinesis in three steps. The first step is CAR formation, when precursor nodes congress to form an intact ring (Wu *et al.*, 2006). Nodes are positioned in the cell middle by positive signals from the nucleus, and by inhibitory signals from the protein kinase Pom1 at cell tips (Bähler and Pringle, 1998; Daga and Chang, 2005; Celton-Morizur *et al.*, 2006; Padte *et al.*, 2006). Both signals converge on the anillin-like scaffold protein Mid1 (Celton-Morizur *et al.,* 2006; Padte *et al.,* 2006*;* Almonacid *et al.*, 2009; Almonacid *et al.*, 2011). The second step is CAR maturation, when additional proteins are recruited to the division site (Wu *et al.*, 2003; Wu *et al.*, 2006; Pollard and Wu, 2010). During maturation, the CAR must be anchored in place to prevent sliding towards cell ends. Several proteins have been implicated in anchoring the CAR: the cell wall synthase Bgs1 (Arasada and Pollard, 2014; G. Cortés *et al.*, 2015; Sethi *et al*., 2016), the membrane-binding protein Cdc15 (Arasada and Pollard, 2014; McDonald *et al.*, 2015; Snider *et al*., 2017), regulators of the lipid $PI(4,5)P_2$ (Snider *et al.*, 2017; Snider *et al.*, 2018), and the scaffolding protein Pxl1 (G. Cortés *et al*., 2015). The third step is CAR constriction, which must be coordinated with septum assembly (Liu *et al.*, 1999; Sipiczki and Bozsik, 2000; Liu *et al.*, 2002). Both CAR constriction and septation contribute to the force required for cytokinesis and cell separation (Jochová *et al.*, 1991; Proctor *et al.*, 2012).

In fission yeast and other systems, protein kinases provide spatial and temporal regulation of cytokinesis. Protein phosphatases, which counter the activity of protein kinases, therefore represent potential regulators of cytokinetic events. In human cells, phosphatases have recently been linked to cytokinesis (Burgess *et al.*, 2010; Cundell *et al.*, 2013). In fission yeast, the phosphatases calcineurin and Clp1 localize to the division site and regulate the timing of cytokinetic events (Trautmann *et al.,* 2001; Mishra *et al.,* 2004; Clifford *et al.*, 2008; Martín-García *et al.*, 2018). Fission yeast mutants in the conserved heterotrimeric phosphatase PP2A have suggested a role for this phosphatase in cytokinesis, but how regulation of PP2A might connect to specific steps in cytokinesis is unclear (Kinoshita *et al.*, 1996; Jiang and Hallberg, 2001; Le Goff *et al.*, 2001; Lahoz *et al.*, 2010; Goyal and Simanis, 2012). PP2A mutants exhibit defects in diverse cellular processes, making it challenging to obtain a clear connection with cytokinesis. PP2A is regulated by a number of upstream factors, which might control specific aspects of PP2A function. We reasoned that mutating these regulators could provide a way to study how this conserved phosphatase regulates cytokinesis without affecting other cellular functions.

In this study, we have identified and characterized cytokinesis defects in cells lacking Sds23, which binds to and inhibits PP2A-related phosphatases (Hanyu *et al.*, 2009; Deng *et al.*, 2017). We found that the CAR assembles off-center in *sds23*Δ mutants, and once assembled slides away from the cell middle due to delayed recruitment of potential anchors. The phenotypes of *sds23*Δ cells are exacerbated when combined with deletion of a second inhibitor of PP2A, Igo1 (Chica *et al.*, 2016), suggesting that Sds23 and Igo1 function together in regulating PP2A-controlled cellular processes.

## Results and Discussion

### *Cells lacking Sds23 divide asymmetrically*

While studying Sds23 in nutrient signaling (Deng *et al.*, 2017), we observed that *sds23*Δ cells divide with off-center septa (Figure 1A). We quantified this defect by measuring the Cell

Half Ratio (Figure 1B, Supplemental Figure 1A) (Snider *et al.*, 2017) and confirmed a significant defect in positioning the division plane for *sds23*Δ cells compared to wild type cells (Figure 1C). We obtained similar results whether Cell Half Ratio was measured by cell length, cross-sectional area, or cell perimeter (Supplemental Figure 1, B and C). At division, *sds23*Δ cells are longer than wild type cells, so we considered the possibility that increased cell length caused the measured division asymmetry. To address this idea, we used a *cdc25-degron-DAmP* (hereafter, *cdc25-dd*) strain, which divides at a similar length to *sds23*Δ (Figure 1A). We found that *cdc25-dd* cells divide as symmetrically as wild type cells, indicating that asymmetric division of *sds23*Δ cells is not due to cell length (Figure 1C). The *sds23*Δ and *cdc25-dd* mutations had additive defects in cell length, but *sds23*Δ *cdc25-dd* double mutant cells displayed the same Cell Half Ratio as *sds23*Δ single mutants (Figure 1C). We conclude that Sds23 regulates the position of the division plane independent of cell size.

***sds23 mutants fail to assemble and to anchor the CAR in the cell middle***

We next investigated the cause of misplaced division planes in *sds23*Δ cells. We monitored the position and timing of CAR assembly using *rlc1-mNeonGreen* (hereafter, *rlc1-mNG*) *sad1-mEGFP* cells. Rlc1 marks the precursor nodes and CAR, and Sad1 marks the spindle pole bodies (SPBs), which provide a clock for cytokinetic events (Wu *et al.*, 2003). CAR formation occurred with the same timing in *sds23*Δ and wild type cells, but was misplaced in *sds23*Δ cells (Figure 2, A and B). Misplaced ring assembly is not due to delocalized Pom1, which remained at cell tips in *sds23*Δ cells (Supplemental Figure 1D), or changes in the localization of Cdr2 nodes, which are precursors to cytokinetic nodes (Supplemental Figure 1E). Thus, the off-center CAR phenotype of *sds23*Δ cells does not reflect changes to Pom1-dependent negative spatial cues.

In addition to Pom1-dependent negative spatial cues, CAR formation also depends on positive spatial cues from the nucleus. Using Cut11-mCherry to mark the nucleus, we performed time-lapse imaging of wild type and *sds23*Δ cells. In wild type cells, the nucleus remained stationary at the center of cells (Figure 2, C and D), consistent with proper medial placement of the CAR in these cells. In *sds23*Δ cells, the nucleus was not stationary at the cell middle, and instead wandered off-center (Figure 2, C and D). Importantly, nuclear positioning and nuclear movement in elongated *cdc25-dd* cells resembled wild type (Figure 2, C and D). Similar results were obtained by visualizing the localization of the SPB over time (Figure 2E). Microtubules (MTs) connected to the nucleus push against the cell ends to position nuclei in the cell middle (Tran et al., 2001; Daga et al., 2006). To determine if defects in MTs were responsible for the increased nuclear movement, we imaged *sds23*Δ cells with fluorescently tagged MTs. We found that MTs in *sds23*Δ cells have increased dwell times at the cell tips when compared to both wild type and *cdc25-dd* cells. (Figure 2F). This difference likely contributes to nuclear wandering and off-center CAR formation through mislocalization of positive spatial cues.

At the molecular level, this positive spatial cue is provided by Mid1, which shuttles between the nucleus and precursor nodes to coordinate spatial cues from these two structures (Bähler *et al*., 1998a; Daga and Chang, 2005; Almonacid *et al*., 2009). Mid1-mNeonGreen displayed reduced levels in the nucleus and the CAR (Figure 2G and Supplemental Figure 2K), although node localization of Mid1 was not obviously impaired (Figure 2G). Strikingly, the cellular protein level of Mid1 was reduced in *sds23*Δ cells, as measured by both whole cell fluorescence and western blot (Figure 2H and Supplemental Figure 1F). Thus, *sds23*Δ cells have

defects in nuclear positioning and in Mid1 regulation. These defects likely lead to misplaced CAR assembly away from the cell middle.

Once assembled, the CAR must be anchored in place during the maturation phase of cytokinesis. In certain mutants, CARs assemble properly but then slide away from the cell middle, resulting in asymmetric division. This defect has been observed in mutants that alter plasma membrane PI(4,5)$P_2$ regulation (Snider *et al.*, 2017; Snider *et al*., 2018), or upon mutation of Cdc15, an essential F-BAR domain protein that might tether the CAR to the plasma membrane (Arasada and Pollard, 2014; McDonald *et al.*, 2015; Snider *et al*., 2017). To determine if ring sliding defects occur in *sds23*Δ cells, we performed time-lapse imaging on *rlc1-mNG sad1-mEGFP* cells. After ring formation, CARs in wild type or elongated *cdc25-dd* cells did not move from their initial position. In contrast, CARs slid away from their initial position in *sds23*Δ cells (Figure 3A). We measured ring displacement (Figure 3B) and found that CARs slid significantly farther in *sds23*Δ cells than in wild type or *cdc25-dd* cells (Figure 3C). In these experiments, CARs slid during the time period corresponding to ring maturation, which occurs after assembly but before constriction. We measured a significantly longer maturation phase in *sds23*Δ versus wild type cells (Figure 3D), indicating that this CAR stage requires Sds23 to proceed normally.

We next tested if this Sds23 function in cell division symmetry connects with PI(4,5)$P_2$ regulation by combining *sds23*Δ with *efr3*Δ. Efr3 is a scaffold for PI-4 kinase, and *efr3*Δ cells were recently shown to exhibit ring sliding (Snider *et al.*, 2017) (Figure 1, A and C). The *sds23*Δ *efr3*Δ double mutant did not show additive defects in division asymmetry (Figure 3E), but this result was difficult to interpret because *sds23*Δ *efr3*Δ double mutant cells lysed at a high frequency (Figure 3F). This synthetic fitness defect suggests that Sds23 may function through a different pathway from PI(4,5)$P_2$ regulation.

***Sds23 is required for timely recruitment of CAR anchors***

Reduced recruitment of proteins that anchor the CAR in place could explain both the ring sliding and extended maturation phase of *sds23*Δ mutant cells. To test this hypothesis, we measured the levels of 22 cytokinesis proteins at the CAR using live-cell microscopy of wild type or *sds23*Δ cells (Supplemental Figure 2, A-V). Several proteins that might contribute to ring anchoring were present in reduced levels at the CAR of *sds23*Δ cells. These proteins include Bgs1, a transmembrane cell wall enzyme, and Imp2 and Rga7, which both contain membrane-binding F-BAR domains (Supplemental Figure 2, A, B and P) (Demeter and Sazer, 1998; Martin-Garcia et al., 2014; Arasada and Pollard, 2015; McDonald et al., 2016). We did not detect altered levels of Cdc15, another F-BAR domain containing protein that is implicated in ring anchoring (Supplemental Figure 2C) (Roberts-Galbraith *et al.*, 2009; McDonald *et al.*, 2015).

Past work has suggested that delayed recruitment of Bgs1, which synthesizes 1,3-beta-glucan for the primary septum, can lead to ring sliding (Arasada and Pollard, 2014). We measured the timing of GFP-Bgs1 recruitment in *sds23*Δ and wild type cells using the SPB clock (Wu *et al.*, 2003). Bgs1 recruitment to the division site was delayed 10-15 minutes in *sds23*Δ compared to wild type cells (Figure 4, A and B), consistent with a similar extension in the maturation phase of cytokinesis in this mutant. We observed similar delays in Imp2-GFP (~5 minutes) (Figure 4, C and D) and Rga7-GFP (~10-15 minutes) (Figure 4, E and F) recruitment in *sds23*Δ cells compared to wild type cells. Such delays were specific to these factors, as other proteins such as Rlc1 were recruited to the CAR with similar kinetics in *sds23*Δ and wild type

cells (Supplemental Figure 1, G and H). We conclude that Sds23 is required for the timely recruitment of specific putative CAR anchoring proteins to prevent ring sliding.

***Genetic interactions between Sds23 and the Greatwall Kinase Pathway***

Sds23 physically associates with PP2A and PP6 phosphatases, and can inhibit PP6 phosphatase activity (Hanyu *et al.*, 2009; Deng *et al.*, 2017). Similar to other organisms, the fission yeast endosulfine protein Igo1 inhibits PP2A activity (Chica *et al.*, 2016). The Greatwall kinase Ppk18 phosphorylates and activates Igo1, raising the possibility that Ppk18-Igo1 and Sds23 might provide dual regulatory arms for PP2A phosphatases (Figure 5A) (Chica *et al.*, 2016). Both *igo1*Δ and *ppk18*Δ mutants alone did not display defects in cell shape, cell length at division, or division symmetry under normal growing conditions, consistent with previous reports (Figure 5, B-E) (Chica *et al.*, 2016). However, combining either mutation with *sds23*Δ led to synthetic defects. First, the percentage of cells with aberrant morphology, specifically bent and curved cells, was increased in the *sds23*Δ *igo1*Δ and *sds23*Δ *ppk18*Δ double mutant cells compared to single mutants (Figure 5C). Second, the double mutants divided at a larger cell size than the single mutants (Figure 5D), consistent with both pathways acting on PP2A to control mitotic entry. Lastly, the Cell Half Ratio was even further reduced for double mutant cells, but we note that the double mutants were not significantly different from *sds23*Δ alone despite this trend (Figure 5E). Taken together, these results suggest that Sds23 and Igo1 share functions related to cell morphology and cell size, but Sds23 plays a more prominent role in cytokinesis. Consistent with this notion, elongating *igo1*Δ by combining with *cdc25-dd* had no effect on division symmetry (Supplemental Figure 3, A-C) and the *sds23*Δ *igo1*Δ did not have additive defects in nuclear movement (Supplemental Figure 3D). Synthetic defects between Sds23 and Ppk18-Igo1 support a broad role for PP2A-family regulators in cell polarity, cell size, and division plane positioning.

***Conclusions***

Our results define a new role for regulation of PP2A in cytokinesis and cell division. Past work has shown that *sds23*Δ cells exhibit increased levels of PP2A activity (Hanyu *et al.*, 2009), and our results show that these cells have defects in regulating key cytokinesis proteins such as Mid1 and Bgs1. These defects likely underlie misplaced assembly of the CAR and its subsequent sliding away from the cell middle. Future experiments will address if these cytokinesis proteins are direct targets of dysregulated PP2A or if their dysregulation occurs downstream of PP2A itself. PP2A has been proposed to counter the SIN in fission yeast (Jiang and Hallberg, 2000; Jiang and Hallberg, 2001; Le Goff *et al.*, 2001; Lahoz *et al.*, 2010), therefore, Sds23 and Igo1 action on PP2A may alter the balance of PP2A versus SIN activity within the cell, leading to the division phenotypes observed in this study. We note that reduced PP2A activity in *ypa2*Δ has been shown to suppress some SIN mutants, but *ypa2*Δ did not correct the Cell Half Ratio of *sds23*Δ cells (Supplemental Figure 3E). In fact, *ypa2*Δ cells alone exhibited a Cell Half Ratio defect, showing that strict regulation of PP2A activity is critical for division plane positioning.

The ability of an intact CAR to slide laterally within the plane of the plasma membrane indicates a remarkable level of structural integrity and stability, even though many components are exhibiting rapid flux as shown by photobleaching experiments (Pelham and Chang, 2002). It seems likely that the CAR is anchored in place by multiple tethers, including the components implicated in this study as well as previous work (Arasada and Pollard, 2014; McDonald *et al.*, 2015; Snider *et al.*, 2017). Such a multi-component anchoring system may facilitate a spatial

control system that is robust during dynamic processes including septum synthesis, vesicle delivery, and CAR constriction.

Our work places this PP2A regulatory network in the growing context of protein phosphatases that control cytokinesis. Given the roles of PP2A in diverse cellular functions, it will be interesting to know how potential cytokinesis targets are regulated with specificity in time and space. The partially overlapping roles of Sds23 and Igo1, as shown by synthetic genetic defects, raise possibilities for dynamic control of cytokinesis by PP2A during cell cycle progression. The Greatwall-endosulfine pathway including Ppk18-Igo1 is best known for regulation of mitotic entry (Mochida *et al.*, 2010; Burgess *et al.*, 2010; Chica *et al.*, 2016), and Sds23 has also been linked to cell cycle progression through phenotypes such as cell size (Ishii *et al*., 1996; Jang *et al*., 1997; Deng *et al*., 2017). These functional connections to the cell cycle suggest that timely regulation of PP2A by these proteins could ensure proper cytokinesis. Both Sds23 and Igo1 are known to be hyperphosphorylated, which may serve to regulate their interactions with PP2A (Hanyu *et al.*, 2009; Chica *et al.*, 2016). We also note that the Ppk18-Igo1 pathway is upregulated during nitrogen stress (Chica *et al.*, 2016), and Sds23 functions in pathways upregulated during glucose depletion and energy stress (Yakura *et al.*, 2006; Hanyu *et al.*, 2009; Jang *et al.*, 2013; Saitoh *et al.*, 2015; Deng *et al.*, 2017). Thus, it will be interesting to determine how these pathways contribute to cytokinesis when cells encounter environmental stresses linked to their functions. Given the conservation of PP2A complexes and functions in yeast through humans, phosphatase regulation by proteins such as those described here might contribute to robust cytokinesis in diverse cell types and organisms.

## Materials and Methods

### *Yeast Strains and Growth*

Standard *S. pombe* media and methods were used (Moreno *et al.*, 1991). Strains used in this study are listed in Supplemental Table 1. Gene tagging and deletion were performed using PCR and homologous recombination (Bähler et al., 1998b), and integrations were verified by colony PCR, microscopy, and/or western blot. To cross the sterile mutant *sds23*Δ*,* a pJK148 plasmid with *sds23+* or *sds23-mNeonGreen+* was integrated at the *leu1* locus of a *sds23*Δ*::natR leu1-32* strain, and *leu1-32 natR* progeny or *natR* progeny lacking mNeonGreen signal were selected from subsequent crosses.

### *Western Blots and Quantification*

For western blots, 2 $OD_{595}$ logarithmic-phase cells were rapidly harvested and snap-frozen. Whole-cell extracts were prepared by resuspending cells in sample buffer (65 mM Tris pH 6.8, 3% SDS, 10% glycerol, 10% 2-mercaptoethanol, 50 mM NaF, 50 mM β-glycerophosphate, 1 mM sodium orthovanadate, and protease inhibitor cocktail) and lysing with acid-washed glass beads (Sigma) in a Mini-beadbeater-16 (BioSpec, Bartlesville, OK; 2 min at maximum speed in cold room). Lysates were briefly centrifuged to pellet insoluble material, and supernatant was isolated as whole cell extract. All samples shown are whole-cell extracts. Western blots were probed with anti-myc (SC-40, Santa Cruz) and anti-cdc2 (SC-53217, Santa Cruz) primary antibodies, then probed with Goat anti-Mouse secondary antibody (LI-COR). Westerns were then developed on an Odyssey CLx Imaging System (LI-COR) and quantified using Image Studio Lite (LI-COR). To quantify Mid1-13myc protein levels, a rectangle was drawn around each band and intensity of the bands was measured after background subtraction for both Mid1-13myc and Cdc2 loading control. Ratio of Mid1-13myc (myc signal) to total protein (Cdc2 signal) was calculated for three independent samples for both wild type and *sds23*Δ cells. Mid1-13myc/Cdc2 ratios for each were normalized to wild-type levels to show relative changes in Mid1 abundance.

### *Microscopy*

All image analysis was performed on ImageJ (National Institutes of Health) (Schneider *et al*., 2012). For Figure 1A and Supplemental Figure 3A, cells were grown at 32˚C, stained with Blankophor (MP Biomedicals), mounted on a glass slide under a coverslip, and middle focal plane images were obtained at room temperature. Imaging was performed on a Deltavision Imaging System (Applied Precision/GE Healthcare), which used a customized Olympus IX-71 inverted wide-field microscope, a Photometrics Cool-SNAP HQ2 camera, Insight solid-state Illumination unit and 1.42 NA Plan Apo 60x oil objective. For Figure 3E, cells were grown at 32˚C, stained with Blankophor, mounted on a glass slide under a coverslip, and middle focal plane images were obtained at room temperature using the Deltavision Imaging System. For Figure 3F, $n \geq 100$ cells were counted, values represent the mean ± SD of two independent experiments. For Supplemental Figure 1D, cells were grown at 32˚C, mounted on a glass slide under a coverslip, and middle focal plane images were acquired at room temperature using the Deltavision Imaging System. For Supplemental Figure 1E, cells were grown at 32˚C, mounted on a glass slide under a coverslip, and z-sectioning was performed with images acquired every 0.5 µm for 6 µm (12 steps). Images were acquired using the Deltavision imaging system and z-stacks were processed by iterative deconvolution in SoftWorx Software (Applied Precision/GE Healthcare). To calculate FWHM, a rectangular ROI of 160 pixels x 48 pixels was drawn around cells that were between 15-17 µm in length and fluorescence profile for Cdr2-mEGFP

was plotted. A Gaussian distribution was fitted to this fluorescence profile for each cell using the Least Squares Regression method in Graphpad Prism, and FWHM was calculated by the following equation: $2*(\sqrt{}(2\ln 2))*SD$, where SD is the standard deviation. Each point represents a single cell (n = 10 cells per strain) and statistical analysis was performed by unpaired t-test with Welch's Correction. For Figure 5B and Supplemental Figure 1A, cells were grown at 32˚C, stained with Blankophor, mounted on a glass slide under a coverslip, and middle focal plane images were obtained using a Nikon Eclipse Ti microscope equipped with an Andor Zyla camera, Perfect Focus and a Tokai Hit stage incubator maintained at 32˚C and using a Plan Apo λ 1.4 NA aperture 60x oil objective. For Figure 5C, n > 200 cells were counted.

For Cell Half Ratio analysis, cell length of each daughter cell was measured from Blankophor stained images using the Angle Tool in ImageJ. The Angle Tool was used to draw a line containing 3 points to accommodate for bent cell shapes, as displayed in Supplemental Figure 1A. Cell Half Ratio was calculated by dividing the short half by the long half. Additionally, Cell Half Ratio was also calculated by using the Freehand Selection tool to trace the perimeter of the daughter cells and measuring cross-sectional area and perimeter. The ratio of the cross-sectional areas or perimeters of the daughter cells resulted in similar trends as the length ratios (compare Figure 1C and Supplemental Figures 1B and 1C), therefore, we concluded that length was sufficient for these measurements and length measurements were used for subsequent Cell Half Ratio analyses (with the exception of Supplemental Figure 1, B and C). For Cell Length at Division analysis, length of septated cells was measured from Blankophor stained images using the Angle Tool in ImageJ (also shown in Supplemental Figure 1A). For all Cell Half Ratio (Length/Perimeter/Area) and Cell Length at Division measurements n ≥ 50 cells were measured (each point represents a single cell) and mean ± SD is displayed for all. For statistical analysis of all Cell Half Ratio and Cell Length at Division graphs, a one-way Anova with Tukey's multiple comparisons test was performed. Unless otherwise indicated, cells were grown at 32˚C in EMM4S for these measurements. For Figures 2A, 2B, 2C, 2D, 2E, 2F, 3A, 3C, 3D, 4, A-F, Supplemental Figure 1G and 1H, and Supplemental Figure 3D cells were imaged at 32˚C using a Andor W1 Spinning Disk Confocal, set up on a Nikon Eclipse Ti inverted microscope stand with Perfect Focus and Tokai Hit stage incubation system using a Plan Apo λ 1.4 NA aperture 60x oil objective. For imaging, ~1 µl of cells were mounted on EMM4S agarose pads (1.4% InCert™ Agarose, Lonza) and sealed under a coverslip with VALAP (Vaseline, Lanolin, Parrafin). For Figure 2B, Cell Half Ratio at the initial time of ring formation, determined by Rlc1-mNeonGreen signal, was measured. Each point represents a single cell (n ≥ 26 cells measured per strain). For Figures 2A and 3D, ring assembly and maturation timing were determined from time-lapse movies of Rlc1-mNeonGreen and Sad1-mEGFP expressing cells that were imaged every 5 minutes. Ring assembly was determined as the time it took from SPB splitting to form an intact CR. Ring maturation was determined as the time between ring assembly and prior to constriction. Each point represents a single cell (n ≥ 19 cells measured per strain). For statistical analysis of Figures 2A and 3D, a one-way ANOVA with Tukey's multiple comparisons was used. For Figures 2G and 2H, cells were grown at 32˚C, mounted on a glass slide under a coverslip, and maximum intensity projections were generated using 0.5-µm focal planes throughout the entire cell (13 steps, 6 µm total). Images were obtained using the Andor W1 Spinning Disk Confocal and a Tokai Hit stage incubator maintained at 32˚C and using a Plan Apo λ 1.45 NA 100x oil objective. For Figure 2H, a one-way ANOVA with Tukey's multiple comparisons was used.

For images in Figure 2D, single focal plane images in the cell middle were acquired every 3 minutes. To measure nuclear movement a line was drawn from the center of the nucleus to the cell tip, and the length of this line was measured at every time point. Nuclear movement (μm/min) was quantified as the average difference between those lengths between every time point, divided by 3 minutes. Each point in Figure 2C and Supplemental Figure 3D is the average for a single cell (n = 10 cells measured per strain). Note that the data in Figure 2C is repeated in Supplemental Figure 3D for comparative purposes. For statistical analysis of nuclear movement, a one-way ANOVA with Tukey's multiple comparisons test was used. For images in Figure 2E, images were acquired every 30 seconds and sum intensity projections were generated using 0.5-μm focal planes of the cell middle (3 steps, 1 μm total). For Figure 2F, cells expressing *nmt1-GFP-atb2* were grown in EMM4S containing 15 μM thiamine to keep cells in repressed conditions for the *nmt1* promoter. Images were acquired every 5 seconds and sum intensity projections were generated using 0.5-μm focal planes of the cell middle (3 steps, 1 μm total) to determine microtubule dwell time at the cell tips (n = 98 microtubule tip dwell times were determined from n ≥ 26 cells per strain). For Figure 2F, a one-way ANOVA with Tukey's multiple comparisons was used. For images in Figure 3A, images were acquired every 5 minutes and sum intensity projections were generated using 0.5-μm focal planes throughout the entire cell (11 steps, 5 μm total). For displacement measurements in Figure 3C, the length of one cell half was measured at ring formation and the length of that same cell half was measured at final ring constriction. The difference between these two values was quantified as the ring displacement (μm) (See Figure 3B schematic). Each dot in Figure 3C corresponds to a single cell (n ≥ 32 cells per strain were measured) and for statistical analysis in Figure 3C a one-way ANOVA with Tukey's multiple comparisons test was used.

For Figures 4A, 4C, 4E, and Supplemental Figure 1G images were acquired every 5 minutes using the Andor W1 Spinning Disk Confocal at 32˚C and sum intensity projections were generated using 0.2-μm focal planes throughout the entire cell (27 steps, 5 μm total) using a Plan Apo λ 1.4 NA 60x oil objective. For Supplemental Figure 2 A-V, cells were imaged in liquid medium under a coverslip, and images were acquired on the Andor W1 Spinning Disk Confocal at 32˚C using a Plan Apo λ 1.4 NA 60x oil objective. Each point represents a single cell. Sum projection images (non-deconvolved) were used for all quantitative analyses in Figure 4, Supplemental Figure 1H, and Supplemental Figure 2. For Figure 4, Supplemental Figure 1H, and Supplemental Figure 2, an ROI corresponding to the cytokinetic ring was drawn to measure integrated density. To measure background signal, the same ROI was moved to a place with no cells and this background signal was subtracted. For statistical analyses in Supplemental Figure 2, unpaired t-tests with Welch's correction were performed and p-values were determined by two-tailed distribution. For all statistical analyses, Graphpad Prism was used. For all statistical analyses, a single asterisk (*) denotes p-values < 0.05, two asterisks (**) indicate p-values < 0.01, three asterisks (***) indicate p-value <0.001 and four asterisks (****) indicate p-value < 0.0001.

**Acknowledgements**

We thank members of the Moseley lab, the Biomolecular Targeting Core (BioMT) (P20-GM113132) and the Imaging Facility at Dartmouth for use of equipment. We also thank Jian-Qiu Wu, Juan Carlos Ribas, Dan McCollum, Phong Tran, Kathy Gould, and Vladimir Sirotkin for sharing strains. This work was supported by grants from the American Cancer Society (RSG-

15-140-01) and the National Institute of General Medical Sciences (R01GM099774) to J.B.M. K.L.S. was supported by a T-32 Training Grant (T32GM008704).

## References

Almonacid, M., Moseley, J.B., Janvore, J., Mayeux, A., Fraisier, V., Nurse, P., and Paoletti, A. (2009). Spatial Control of Cytokinesis by Cdr2 Kinase and Mid1/Anillin Nuclear Export. Current Biology *19*, 961–966.

Almonacid, M., Celton-Morizur, S., Jakubowski, J.L., Dingli, F., Loew, D., Mayeux, A., Chen, J.-S., Gould, K.L., Clifford, D.M., and Paoletti, A. (2011). Temporal control of contractile ring assembly by Plo1 regulation of myosin II recruitment by Mid1/anillin. Curr. Biol. *21*, 473–479.

Arasada, R., and Pollard, T.D. (2014). Contractile Ring Stability in S. pombe Depends on F-BAR Protein Cdc15p and Bgs1p Transport from the Golgi Complex. Cell Reports *8*, 1533–1544.

Arasada, R., and Pollard, T.D. (2015). A role for F-BAR protein Rga7p during cytokinesis in S. pombe. Journal of Cell Science *128*, 2259–2268.

Bähler, J., and Pringle, J.R. (1998). Pom1p, a fission yeast protein kinase that provides positional information for both polarized growth and cytokinesis. Genes Dev. *12*, 1356–1370.

Bähler, J., Steever, A.B., Wheatley, S., Wang, Y. l, Pringle, J.R., Gould, K.L., and McCollum, D. (1998a). Role of polo kinase and Mid1p in determining the site of cell division in fission yeast. J. Cell Biol. *143*, 1603–1616.

Bähler, J., Wu, J.Q., Longtine, M.S., Shah, N.G., McKenzie, A., Steever, A.B., Wach, A., Philippsen, P., and Pringle, J.R. (1998b). Heterologous modules for efficient and versatile PCR-based gene targeting in Schizosaccharomyces pombe. Yeast *14*, 943–951.

Burgess, A., Vigneron, S., Brioudes, E., Labbé, J.-C., Lorca, T., and Castro, A. (2010). Loss of human Greatwall results in G2 arrest and multiple mitotic defects due to deregulation of the cyclin B-Cdc2/PP2A balance. Proceedings of the National Academy of Sciences *107*, 12564–12569.

Celton-Morizur, S., Racine, V., Sibarita, J.-B., and Paoletti, A. (2006). Pom1 kinase links division plane position to cell polarity by regulating Mid1p cortical distribution. J. Cell. Sci. *119*, 4710–4718.

Chang, F., Woollard, A., and Nurse, P. (1996). Isolation and characterization of fission yeast mutants defective in the assembly and placement of the contractile actin ring. J. Cell. Sci. *109 ( Pt 1)*, 131–142.

Chica, N., Rozalén, A.E., Pérez-Hidalgo, L., Rubio, A., Novak, B., and Moreno, S. (2016). Nutritional Control of Cell Size by the Greatwall-Endosulfine-PP2A·B55 Pathway. Current Biology *26*, 319–330.

Clifford, D.M., Wolfe, B.A., Roberts-Galbraith, R.H., McDonald, W.H., Yates, J.R., and Gould, K.L. (2008). The Clp1/Cdc14 phosphatase contributes to the robustness of cytokinesis by association with anillin-related Mid1. J. Cell Biol. *181*, 79–88.

Cundell, M.J., Bastos, R.N., Zhang, T., Holder, J., Gruneberg, U., Novak, B., and Barr, F.A. (2013). The BEG (PP2A-B55/ENSA/Greatwall) Pathway Ensures Cytokinesis follows Chromosome Separation. Molecular Cell *52*, 393–405.

Daga, R.R., and Chang, F. (2005). Dynamic positioning of the fission yeast cell division plane. Proceedings of the National Academy of Sciences *102*, 8228–8232.

Daga, R.R., Yonetani, A., and Chang, F. (2006). Asymmetric microtubule pushing forces in nuclear centering. Curr. Biol. *16*, 1544–1550.

Demeter, J., and Sazer, S. (1998). imp2, a new component of the actin ring in the fission yeast Schizosaccharomyces pombe. J. Cell Biol. *143*, 415–427.

Deng, L., Lee, M.E., Schutt, K.L., and Moseley, J.B. (2017). Phosphatases Generate Signal Specificity Downstream of Ssp1 Kinase in Fission Yeast. Mol. Cell. Biol. *37*.

G. Cortés, J.C., Pujol, N., Sato, M., Pinar, M., Ramos, M., Moreno, B., Osumi, M., Ribas, J.C., and Pérez, P. (2015). Cooperation between Paxillin-like Protein Pxl1 and Glucan Synthase Bgs1 Is Essential for Actomyosin Ring Stability and Septum Formation in Fission Yeast. PLOS Genetics *11*, e1005358.

Goyal, A., and Simanis, V. (2012). Characterization of *ypa1* and *ypa2* , the *Schizosaccharomyces pombe* Orthologs of the Peptidyl Proyl Isomerases That Activate PP2A, Reveals a Role for Ypa2p in the Regulation of Cytokinesis. Genetics *190*, 1235–1250.

Hanyu, Y., Imai, K.K., Kawasaki, Y., Nakamura, T., Nakaseko, Y., Nagao, K., Kokubu, A., Ebe, M., Fujisawa, A., Hayashi, T., et al. (2009). *Schizosaccharomyces pombe* cell division cycle under limited glucose requires Ssp1 kinase, the putative CaMKK, and Sds23, a PP2A-related phosphatase inhibitor. Genes to Cells *14*, 539–554.

Ishii, K., Kumada, K., Toda, T., and Yanagida, M. (1996). Requirement for PP1 phosphatase and 20S cyclosome/APC for the onset of anaphase is lessened by the dosage increase of a novel gene sds23+. EMBO J. *15*, 6629–6640.

Jang, Y.J., Won, M., Chung, K.S., Kim, D.U., Hoe, K.L., Park, C., and Yoo, H.S. (1997). A novel protein, Psp1, essential for cell cycle progression of Schizosaccharomyces pombe is phosphorylated by Cdc2-Cdc13 upon entry into G0-like stationary phase of cell growth. J. Biol. Chem. *272*, 19993–20002.

Jang, Y.-J., Won, M., and Yoo, H.-S. (2013). Phosphorylations of Sds23/Psp1/Moc1 by stress-activated kinase and cAMP-dependent kinase are essential for regulating cell viability in prolonged stationary phase: Sds23 phosphorylation and viability in stationary phase. Yeast n/a-n/a.

Jiang, W., and Hallberg, R.L. (2000). Isolation and characterization of par1(+) and par2(+): two Schizosaccharomyces pombe genes encoding B' subunits of protein phosphatase 2A. Genetics *154*, 1025–1038.

Jiang, W., and Hallberg, R.L. (2001). Correct regulation of the septation initiation network in Schizosaccharomyces pombe requires the activities of par1 and par2. Genetics *158*, 1413–1429.

Jochová, J., Rupes, I., and Streiblová, E. (1991). F-actin contractile rings in protoplasts of the yeast Schizosaccharomyces. Cell Biol. Int. Rep. *15*, 607–610.

Kinoshita, K., Nemoto, T., Nabeshima, K., Kondoh, H., Niwa, H., and Yanagida, M. (1996). The regulatory subunits of fission yeast protein phosphatase 2A (PP2A) affect cell morphogenesis, cell wall synthesis and cytokinesis. Genes Cells *1*, 29–45.

Lahoz, A., Alcaide-Gavilán, M., Daga, R.R., and Jimenez, J. (2010). Antagonistic roles of PP2A-Pab1 and Etd1 in the control of cytokinesis in fission yeast. Genetics *186*, 1261–1270.

Laplante, C., Huang, F., Tebbs, I.R., Bewersdorf, J., and Pollard, T.D. (2016). Molecular organization of cytokinesis nodes and contractile rings by super-resolution fluorescence microscopy of live fission yeast. Proceedings of the National Academy of Sciences *113*, E5876–E5885.

Le Goff, X., Buvelot, S., Salimova, E., Guerry, F., Schmidt, S., Cueille, N., Cano, E., and Simanis, V. (2001). The protein phosphatase 2A B'-regulatory subunit par1p is implicated in regulation of the S. pombe septation initiation network. FEBS Lett. *508*, 136–142.

Liu, J., Wang, H., McCollum, D., and Balasubramanian, M.K. (1999). Drc1p/Cps1p, a 1,3-beta-glucan synthase subunit, is essential for division septum assembly in Schizosaccharomyces pombe. Genetics *153*, 1193–1203.

Liu, J., Tang, X., Wang, H., Oliferenko, S., and Balasubramanian, M.K. (2002). The localization of the integral membrane protein Cps1p to the cell division site is dependent on the actomyosin ring and the septation-inducing network in Schizosaccharomyces pombe. Mol. Biol. Cell *13*, 989–1000.

Martin-Garcia, R., Coll, P.M., and Perez, P. (2014). F-BAR domain protein Rga7 collaborates with Cdc15 and Imp2 to ensure proper cytokinesis in fission yeast. Journal of Cell Science *127*, 4146–4158.

Martín-García, R., Arribas, V., Coll, P.M., Pinar, M., Viana, R.A., Rincón, S.A., Correa-Bordes, J., Ribas, J.C., and Pérez, P. (2018). Paxillin-Mediated Recruitment of Calcineurin to the Contractile Ring Is Required for the Correct Progression of Cytokinesis in Fission Yeast. Cell Reports *25*, 772-783.e4.

McDonald, N.A., Vander Kooi, C.W., Ohi, M.D., and Gould, K.L. (2015). Oligomerization but Not Membrane Bending Underlies the Function of Certain F-BAR Proteins in Cell Motility and Cytokinesis. Developmental Cell *35*, 725–736.

McDonald, N.A., Takizawa, Y., Feoktistova, A., Xu, P., Ohi, M.D., Vander Kooi, C.W., and Gould, K.L. (2016). The Tubulation Activity of a Fission Yeast F-BAR Protein Is Dispensable for Its Function in Cytokinesis. Cell Reports *14*, 534–546.

McDonald, N.A., Lind, A.L., Smith, S.E., Li, R., and Gould, K.L. (2017). Nanoscale architecture of the Schizosaccharomyces pombe contractile ring. ELife *6*.

Mishra, M., Karagiannis, J., Trautmann, S., Wang, H., McCollum, D., and Balasubramanian, M.K. (2004). The Clp1p/Flp1p phosphatase ensures completion of cytokinesis in response to minor perturbation of the cell division machinery in Schizosaccharomyces pombe. J. Cell. Sci. *117*, 3897–3910.

Mochida, S., Maslen, S.L., Skehel, M., and Hunt, T. (2010). Greatwall phosphorylates an inhibitor of protein phosphatase 2A that is essential for mitosis. Science *330*, 1670–1673.

Moreno, S., Klar, A., and Nurse, P. (1991). Molecular genetic analysis of fission yeast Schizosaccharomyces pombe. Meth. Enzymol. *194*, 795–823.

Padte, N.N., Martin, S.G., Howard, M., and Chang, F. (2006). The cell-end factor pom1p inhibits mid1p in specification of the cell division plane in fission yeast. Curr. Biol. *16*, 2480–2487.

Pelham, R.J., and Chang, F. (2002). Actin dynamics in the contractile ring during cytokinesis in fission yeast. Nature *419*, 82–86.

Piekny, A.J., and Glotzer, M. (2008). Anillin Is a Scaffold Protein That Links RhoA, Actin, and Myosin during Cytokinesis. Current Biology *18*, 30–36.

Pollard, T.D., and Wu, J.-Q. (2010). Understanding cytokinesis: lessons from fission yeast. Nat. Rev. Mol. Cell Biol. *11*, 149–155.

Proctor, S.A., Minc, N., Boudaoud, A., and Chang, F. (2012). Contributions of turgor pressure, the contractile ring, and septum assembly to forces in cytokinesis in fission yeast. Curr. Biol. *22*, 1601–1608.

Roberts-Galbraith, R.H., Chen, J.-S., Wang, J., and Gould, K.L. (2009). The SH3 domains of two PCH family members cooperate in assembly of the *Schizosaccharomyces pombe* contractile ring. The Journal of Cell Biology *184*, 113–127.

Saitoh, S., Mori, A., Uehara, L., Masuda, F., Soejima, S., and Yanagida, M. (2015). Mechanisms of expression and translocation of major fission yeast glucose transporters regulated by CaMKK/phosphatases, nuclear shuttling, and TOR. Mol. Biol. Cell *26*, 373–386.

Schneider, C.A., Rasband, W.S., and Eliceiri, K.W. (2012). NIH Image to ImageJ: 25 years of image analysis. Nat. Methods *9*, 671–675.

Sethi, K., Palani, S., Cortés, J.C.G., Sato, M., Sevugan, M., Ramos, M., Vijaykumar, S., Osumi, M., Naqvi, N.I., Ribas, J.C., et al. (2016). A New Membrane Protein Sbg1 Links the Contractile Ring Apparatus and Septum Synthesis Machinery in Fission Yeast. PLOS Genetics *12*, e1006383.

Sipiczki, M., and Bozsik, A. (2000). The use of morphomutants to investigate septum formation and cell separation in Schizosaccharomyces pombe. Arch. Microbiol. *174*, 386–392.

Snider, C.E., Willet, A.H., Chen, J.-S., Arpağ, G., Zanic, M., and Gould, K.L. (2017). Phosphoinositide-mediated ring anchoring resists perpendicular forces to promote medial cytokinesis. The Journal of Cell Biology *216*, 3041–3050.

Snider, C.E., Willet, A.H., Brown, H.T., and Gould, K.L. (2018). Analysis of the contribution of phosphoinositides to medial septation in fission yeast highlights the importance of PI(4,5)$P_2$ for medial contractile ring anchoring. Molecular Biology of the Cell *29*, 2148–2155.

Sohrmann, M., Fankhauser, C., Brodbeck, C., and Simanis, V. (1996). The dmf1/mid1 gene is essential for correct positioning of the division septum in fission yeast. Genes & Development *10*, 2707–2719.

Tran, P.T., Marsh, L., Doye, V., Inoué, S., and Chang, F. (2001). A mechanism for nuclear positioning in fission yeast based on microtubule pushing. J. Cell Biol. *153*, 397–411.

Trautmann, S., Wolfe, B.A., Jorgensen, P., Tyers, M., Gould, K.L., and McCollum, D. (2001). Fission yeast Clp1p phosphatase regulates G2/M transition and coordination of cytokinesis with cell cycle progression. Curr. Biol. *11*, 931–940.

Wu, J.-Q., Kuhn, J.R., Kovar, D.R., and Pollard, T.D. (2003). Spatial and temporal pathway for assembly and constriction of the contractile ring in fission yeast cytokinesis. Dev. Cell *5*, 723–734.

Wu, J.-Q., Sirotkin, V., Kovar, D.R., Lord, M., Beltzner, C.C., Kuhn, J.R., and Pollard, T.D. (2006). Assembly of the cytokinetic contractile ring from a broad band of nodes in fission yeast. The Journal of Cell Biology *174*, 391–402.

Yakura, M., Ishikura, Y., Adachi, Y., and Kawamukai, M. (2006). Involvement of Moc1 in Sexual Development and Survival of *Schizosaccharomyces pombe*. Bioscience, Biotechnology, and Biochemistry *70*, 1740–1749.

## Figure Legends

**Figure 1. *sds23*Δ cells divide asymmetrically.** (A) Representative images of cells of the indicated strains with cell wall stain. Inset is mean cell length at division ± standard deviation (SD). Scale bar 5 μm. (B) Schematic depicting calculation of Cell Half Ratio. (C) Cell Half Ratios of the indicated strains as a measure of division asymmetry. ** indicates p-value < 0.01, **** indicates p-value < 0.0001.

**Figure 2. Defects in nuclear positioning and ring assembly in *sds23*Δ cells.** (A) Duration of CAR assembly in wild type versus *sds23*Δ cells. (B) Cell Half Ratio at time of ring assembly for the indicated strains. **** indicates p-value < 0.0001. (C) Quantification of nuclear movement as a function of time for the indicated strains. (D) Montages displaying two representative cells of the indicated strains with Cut11-mCherry signal overlaid onto DIC images to show the cell tips. Scale bar 8 μm, 3-minute intervals. (E) Timelapse montages displaying representative *sds23*Δ and *cdc25-dd* cells expressing mCherry-Atb2 and Sid4-GFP. The dotted line is initial SPB position. Scale bar 2 μm, 30-second intervals. (F) Quantification of microtubule dwell time at the cell tip in wild type, *sds23*Δ and *cdc25-dd* cells. (G) DIC and middle focal plane inverted fluorescence images of two representative wild type, *sds23*Δ, and *cdc25-dd* cells expressing Mid1-mNeonGreen. Scale bar 8 μm. (H) Quantification of Mid1-mNeonGreen whole cell fluorescence in wild type, *sds23*Δ, and *cdc25-dd* cells.

**Figure 3. CAR sliding in *sds23*Δ cells.** (A) Timelapse montages displaying a representative wild type, *sds23*Δ, and *cdc25-dd* cell expressing Rlc1-mNeonGreen and Sad1-mEGFP, overlaid onto DIC images to visualize the cell tips. Time 0 is SPB splitting. The dotted line is initial ring position. Fluorescence images are sum projections. Scale bar 8 μm. (B) Schematic depicting ring displacement measurement. (C) Quantification of cytokinetic ring displacement. **** indicates p-value < 0.0001. (D) Duration of CAR maturation in wild type versus *sds23*Δ cells. (E) Cell Half Ratios of the indicated strains. (F) Quantification of the percentage of dead cells observed in the indicated strains. Mean ± SD.

**Figure 4. Delayed recruitment of CAR anchors in *sds23*Δ cells.** (A) Timelapse images of GFP-Bgs1 recruitment in wild type versus *sds23*Δ cells. Images are inverted fluorescence of sum projections. Time "0" indicates SPB splitting as determined by Sad1 signal. Note, a 561 nm laser was used to image Sad1-mCherry in the GFP-Bgs1 and Rga7-mEGFP strains, but only the signal from the 488 nm laser is shown. Scale bar 8 μm. (B) Quantification of GFP-Bgs1 recruitment during cytokinesis in wild type versus *sds23*Δ cells. (C) Timelapse images for Imp2-mEGFP recruitment, as in panel A. (D) Quantification of Imp2-mEGFP, as in panel B. (E) Timelapse images for Rga7-mEGFP recruitment, as in panel A. (F) Quantification of Rga7-mEGFP recruitment, as in panel B.

**Figure 5. Genetic interactions between Sds23 and Ppk18-Igo1.** (A) Schematic depicting Igo1 and Sds23 interactions with Protein Phosphatase 2A (PP2A). (B) Representative images of cells of the indicated strains with cell wall stain. Scale bar 8 μm. (C) Quantification of bent cell shape phenotype for the indicated strains. (D) Cell length at division for the indicated strains. (E) Cell Half Ratios of the indicated strains. **** indicates p-value < 0.0001.

**Supplemental Figure 1. Distribution of nodes and myosin recruitment are unaffected in *sds23*Δ.** (A) Image of *sds23*Δ *igo1*Δ cells with cell wall stain to demonstrate use of the "Angle tool" in ImageJ. (B) Top: Schematic depicting Cell Half Ratio by measuring cross-sectional area of cell halves. Bottom: Cell Half Ratio of the indicated strains. **** indicates p-value < 0.0001. (C) Top: Schematic depicting Cell Half Ratio by measuring perimeter of cell halves. Bottom: Cell Half Ratio of the indicated strains. (D) Inverted fluorescence images of Pom1-mEGFP in wild type and *sds23*Δ cells. Scale bar 5 μm. (E) Top: Inverted max projection images of *cdc25-dd* and *sds23*Δ cells expressing Cdr2-mEGFP. Scale bar 8 μm. Bottom: Full-Width Half Maximum (FWHM) of Cdr2-mEGFP signal comparing spread of nodes in *cdc25-dd* and *sds23*Δ cells. (F) Top: Western blot displaying Mid1-13myc in wild type and *sds23*Δ cells. Bottom: Quantification of normalized band intensity for Mid1-13myc levels. (G) Time lapse images of wild type and *sds23*Δ cells expressing Rlc1-mNG and Sad1-mEGFP. Images are inverted fluorescence of sum projections. Scale bar 8 μm. (H) Quantification of Rlc1-mNG over time for wild type and *sds23*Δ.

**Supplemental Figure 2. Screen for localization defects for putative CAR anchor proteins.** (A-V) Quantification of the indicated CAR proteins in wild type and *sds23*Δ cells. * indicates p-value < 0.05, ** indicates p-value < 0.01, *** indicates p-value < 0.001, and **** indicates p-value < 0.0001.

**Supplemental Figure 3. Elongating *igo1*Δ cells does not cause cytokinesis defects.** (A) Representative images of cells of the indicated strains with cell wall stain. Scale bar 5 μm. (B) Cell length at division for the indicated strains. (C) Cell Half Ratios of the indicated strains. (D) Quantification of nuclear movement as a function of time for the indicated strains, data from Figure 2C (wild type, *sds23*Δ, *cdc25-dd*) is displayed again for comparison. **** indicates p-value < 0.0001. (E) Cell Half Ratios of the indicated strains. * indicates p-value < 0.05, ** indicates p-value < 0.01.

**Supplemental Table 1. Strains used in this study.**

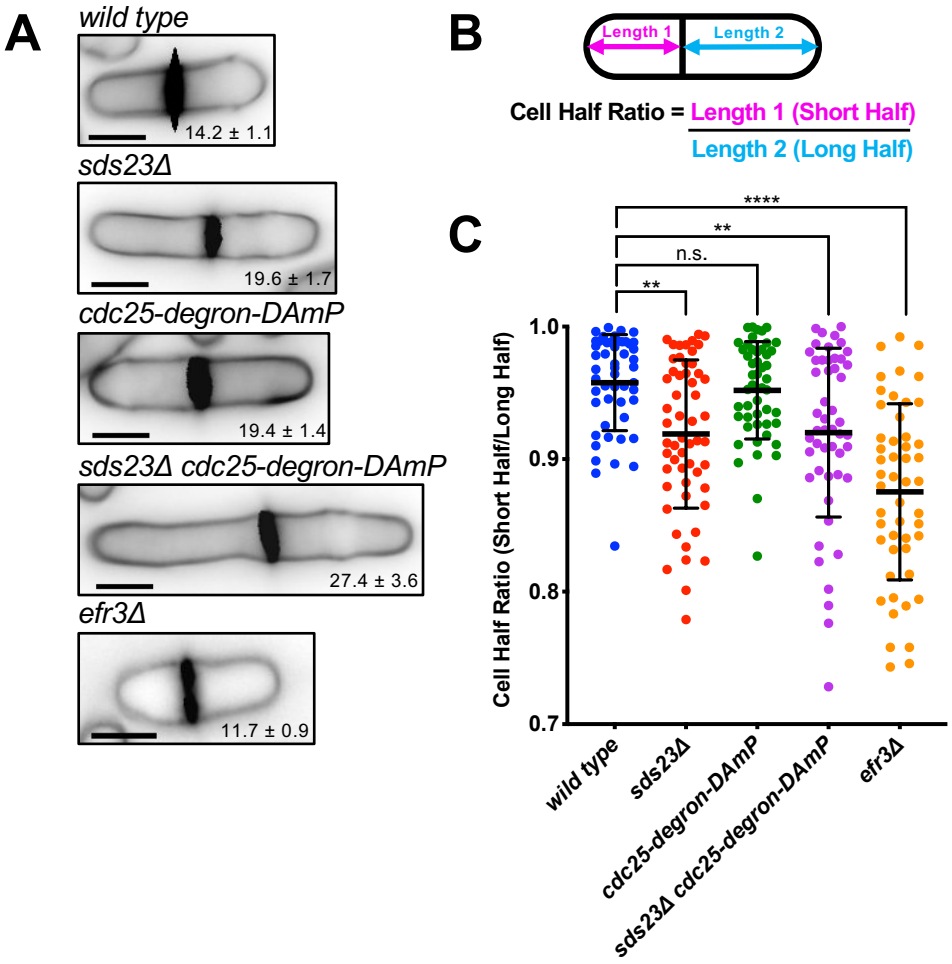


**Figure 1**

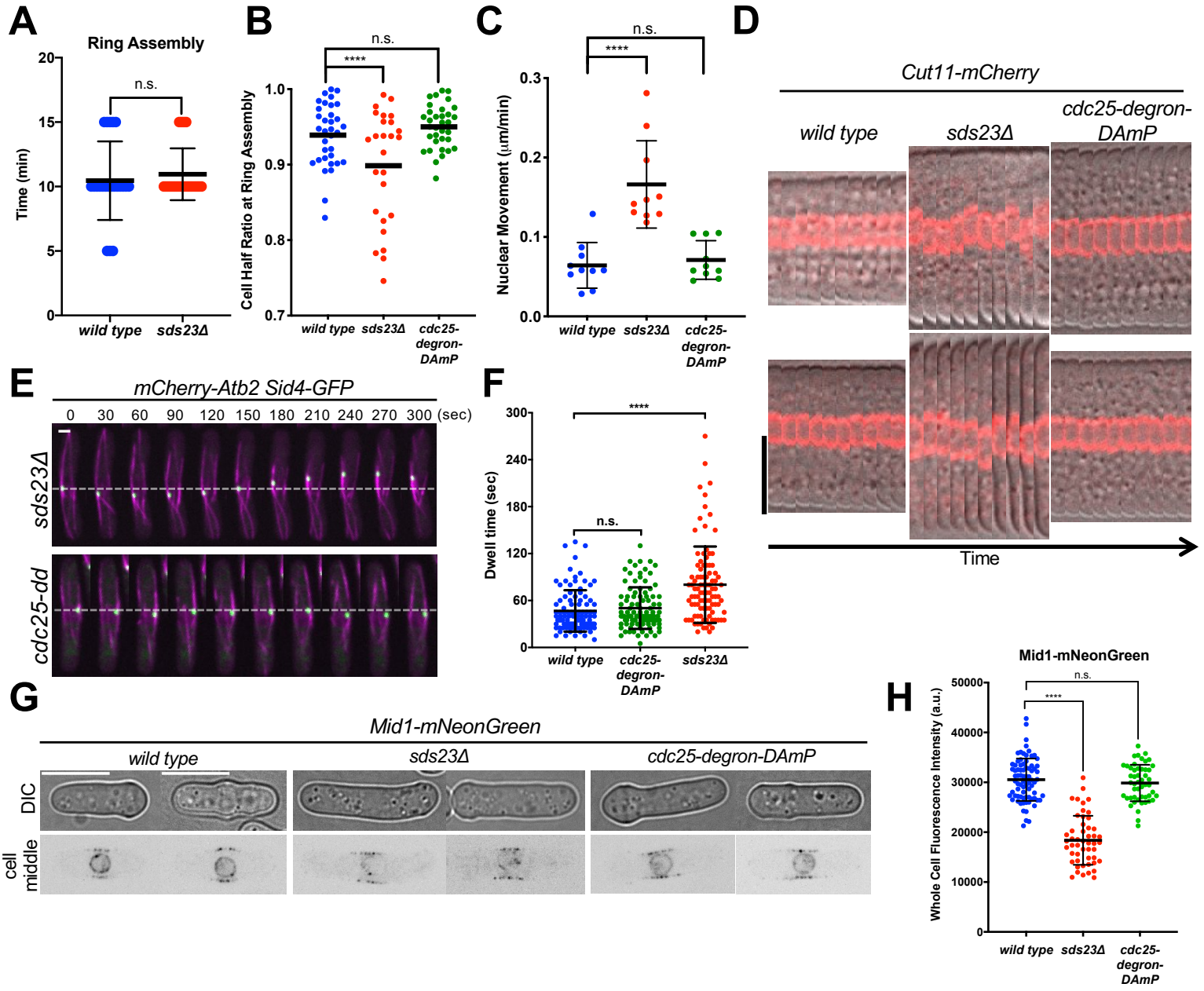
A
Ring Assembly
Time (min)
n.s.
wild type
sds23Δ
B
Cell Half Ratio at Ring Assembly
n.s.
****
wild type
sds23Δ
cdc25-degron-DAmP
C
Nuclear Movement (μm/min)
n.s.
****
wild type
sds23Δ
cdc25-degron-DAmP
D
Cut11-mCherry
wild type
sds23Δ
cdc25-degron-DAmP
Time
E
mCherry-Atb2 Sid4-GFP
0 30 60 90 120 150 180 210 240 270 300 (sec)
sds23Δ
cdc25-dd
F
Dwell time (sec)
****
n.s.
wild type
cdc25-degron-DAmP
sds23Δ
G
Mid1-mNeonGreen
wild type
sds23Δ
cdc25-degron-DAmP
DIC
cell middle
H
Mid1-mNeonGreen
Whole Cell Fluorescence Intensity (a.u.)
n.s.
****
wild type
sds23Δ
cdc25-degron-DAmP

**Figure 2**

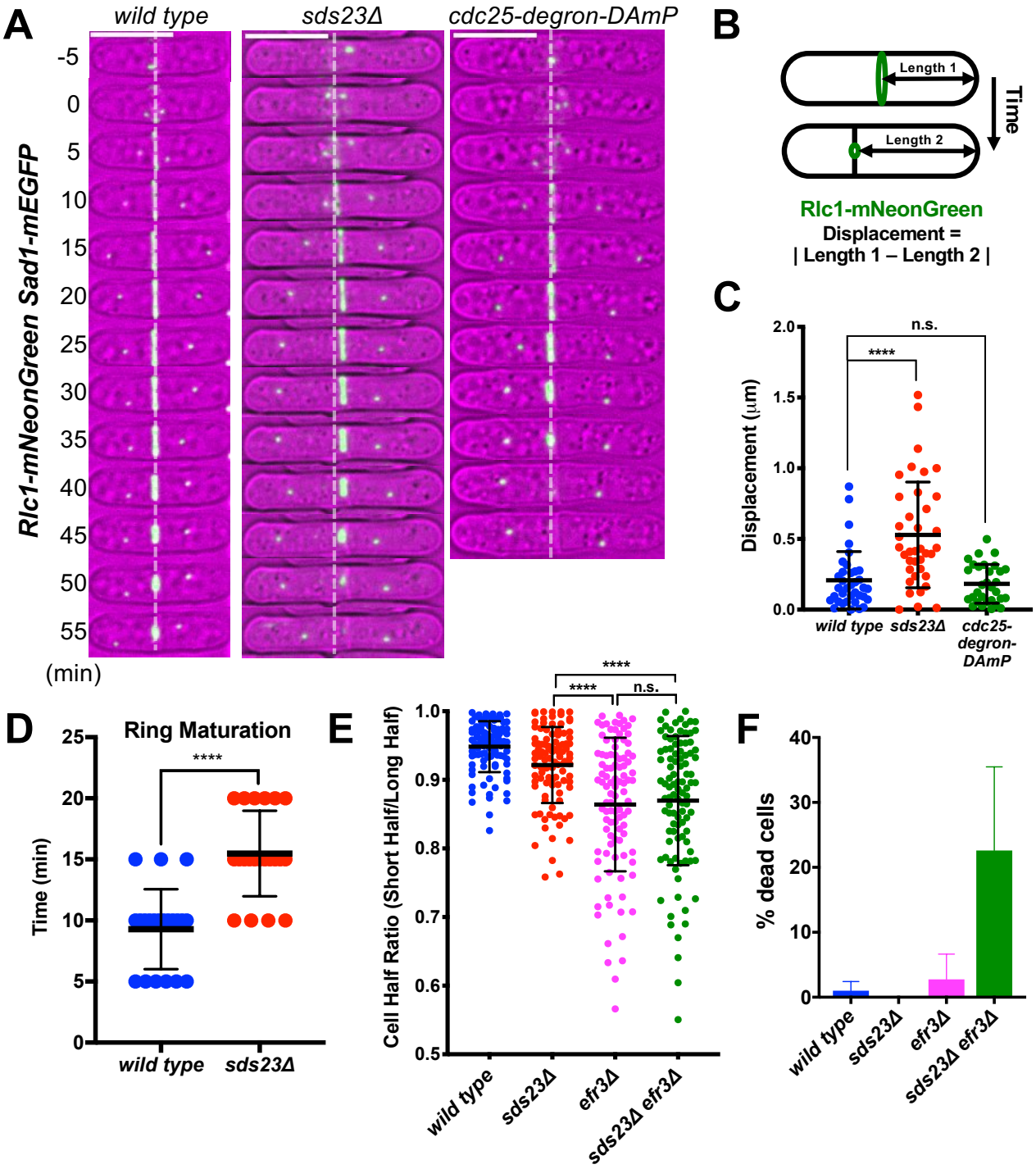
A
wild type
sds23Δ
cdc25-degron-DAmP
Rlc1-mNeonGreen Sad1-mEGFP
-5
0
5
10
15
20
25
30
35
40
45
50
55
(min)
B
Length 1
Length 2
Time
Rlc1-mNeonGreen
Displacement =
| Length 1 – Length 2 |
C
Displacement (μm)
2.0
1.5
1.0
0.5
0.0
n.s.
****
wild type
sds23Δ
cdc25-degron-DAmP
D
Ring Maturation
****
Time (min)
25
20
15
10
5
0
wild type
sds23Δ
E
Cell Half Ratio (Short Half/Long Half)
1.0
0.9
0.8
0.7
0.6
0.5
****
****
n.s.
wild type
sds23Δ
efr3Δ
sds23Δ efr3Δ
F
% dead cells
40
30
20
10
0
wild type
sds23Δ
efr3Δ
sds23Δ efr3Δ

**Figure 3**

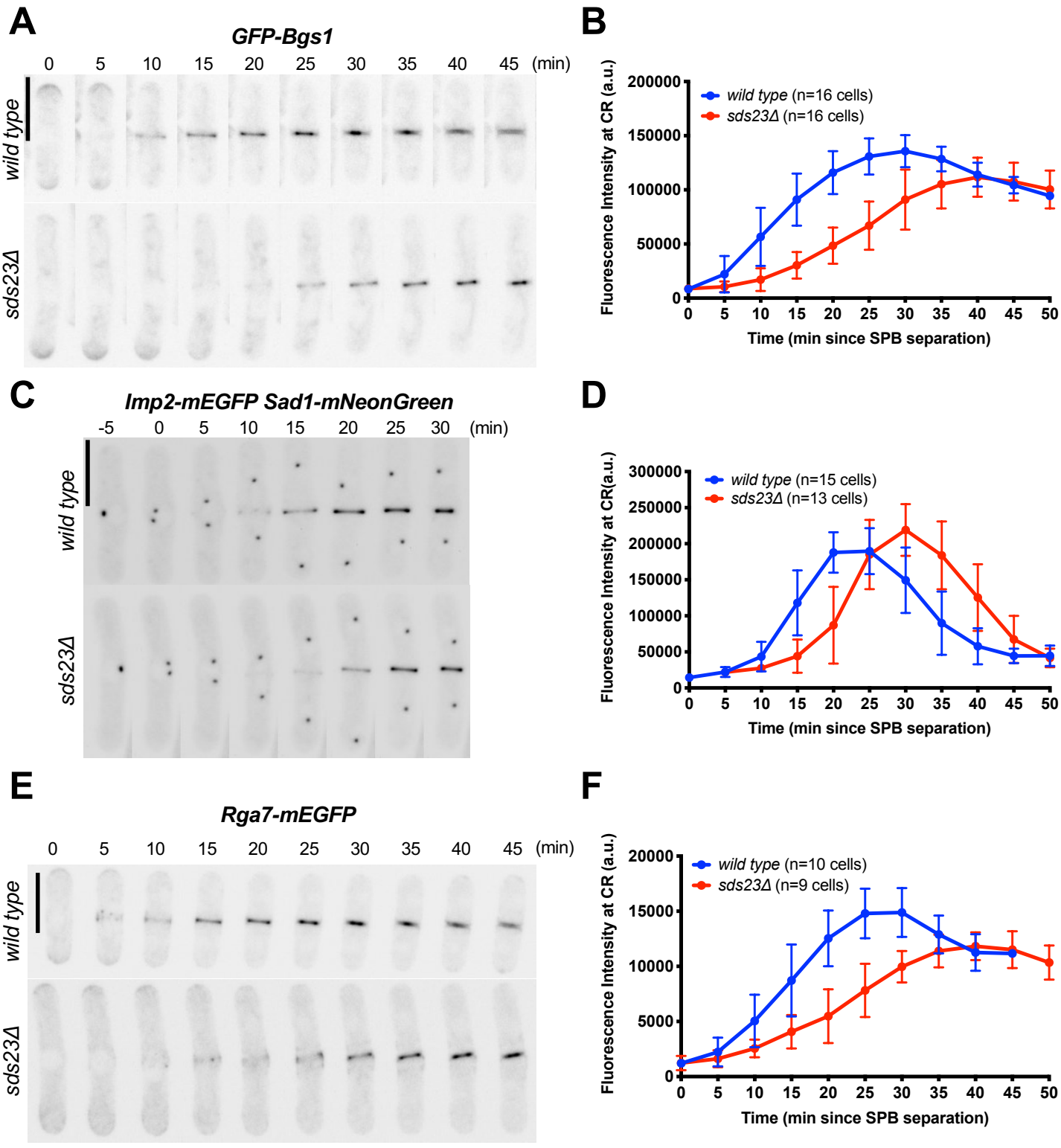
A
GFP-Bgs1
0 5 10 15 20 25 30 35 40 45 (min)
wild type
sds23Δ
B
Fluorescence Intensity at CR (a.u.)
wild type (n=16 cells)
sds23Δ (n=16 cells)
Time (min since SPB separation)
C
Imp2-mEGFP Sad1-mNeonGreen
-5 0 5 10 15 20 25 30 (min)
wild type
sds23Δ
D
Fluorescence Intensity at CR(a.u.)
wild type (n=15 cells)
sds23Δ (n=13 cells)
Time (min since SPB separation)
E
Rga7-mEGFP
0 5 10 15 20 25 30 35 40 45 (min)
wild type
sds23Δ
F
Fluorescence Intensity at CR (a.u.)
wild type (n=10 cells)
sds23Δ (n=9 cells)
Time (min since SPB separation)

**Figure 4**

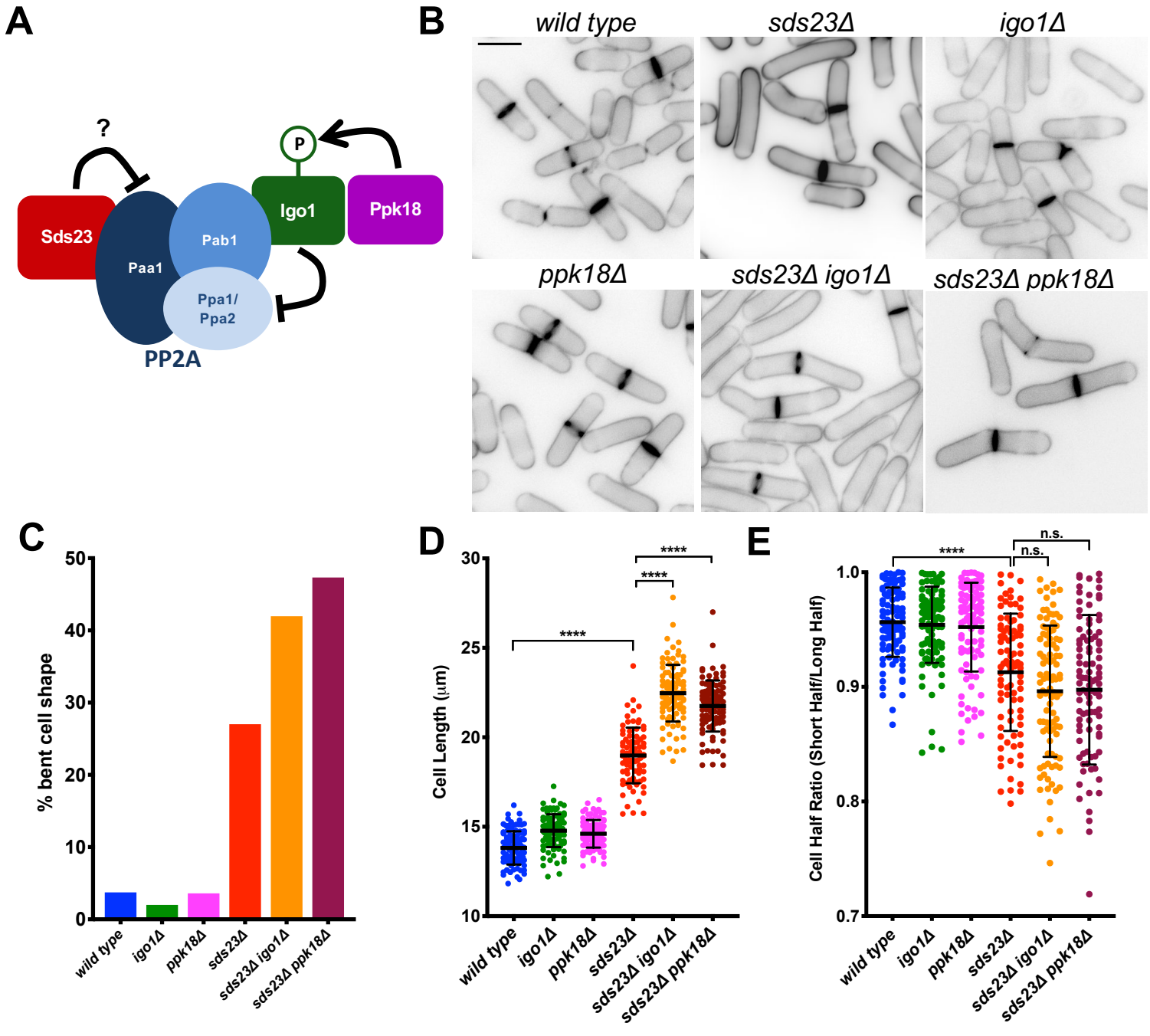
A
?
P
Sds23
Paa1
Pab1
Igo1
Ppk18
Ppa1/
Ppa2
PP2A
B
wild type
sds23Δ
igo1Δ
ppk18Δ
sds23Δ igo1Δ
sds23Δ ppk18Δ
C
% bent cell shape
0
10
20
30
40
50
wild type
igo1Δ
ppk18Δ
sds23Δ
sds23Δ igo1Δ
sds23Δ ppk18Δ
D
Cell Length (μm)
10
15
20
25
30
****
****
****
wild type
igo1Δ
ppk18Δ
sds23Δ
sds23Δ igo1Δ
sds23Δ ppk18Δ
E
Cell Half Ratio (Short Half/Long Half)
0.7
0.8
0.9
1.0
****
n.s.
n.s.
wild type
igo1Δ
ppk18Δ
sds23Δ
sds23Δ igo1Δ
sds23Δ ppk18Δ

**Figure 5**

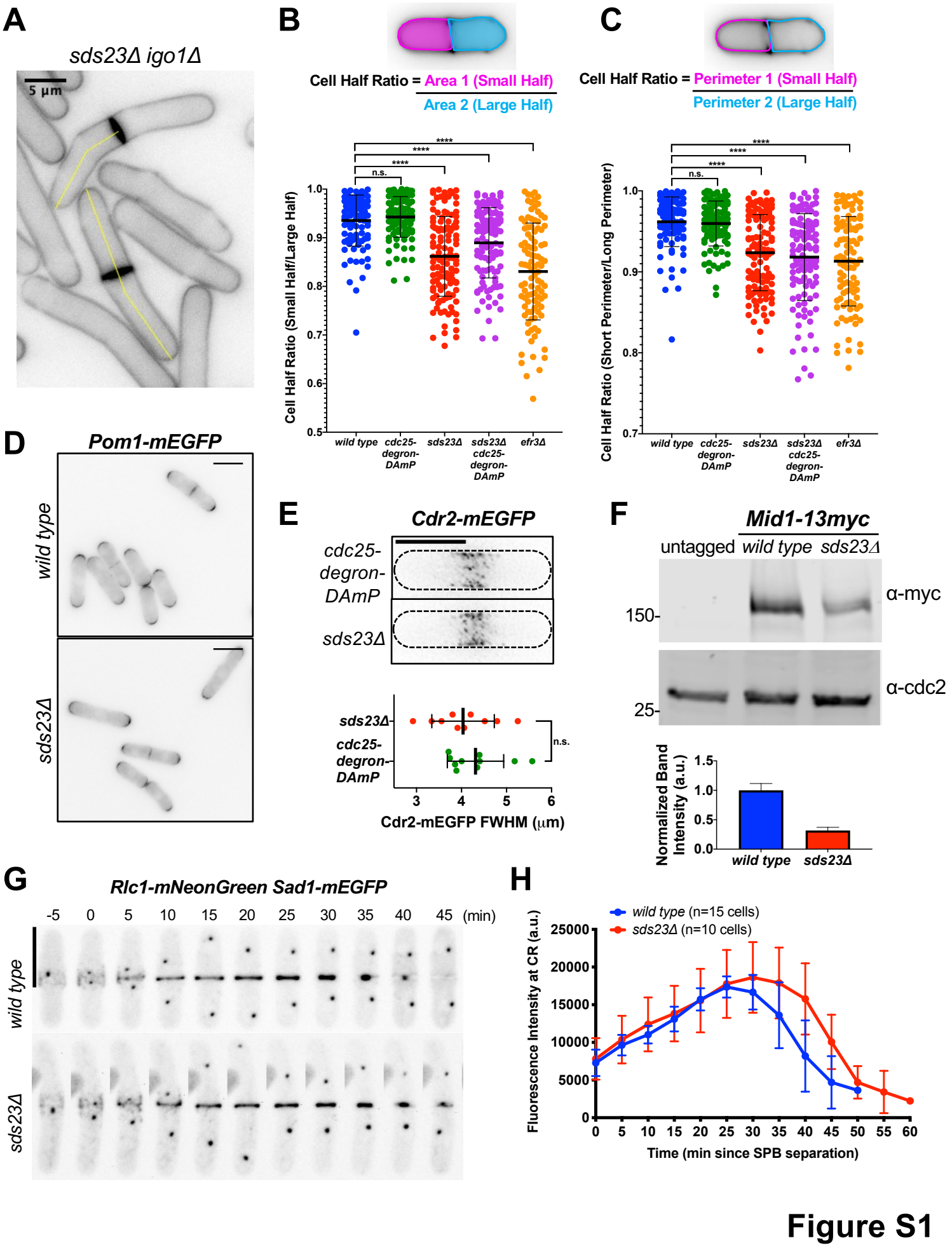
A
sds23Δ igo1Δ
5 μm
B
Cell Half Ratio = Area 1 (Small Half) / Area 2 (Large Half)
Cell Half Ratio (Small Half/Large Half)
wild type
cdc25-degron-DAmP
sds23Δ
sds23Δ cdc25-degron-DAmP
efr3Δ
n.s.
****
C
Cell Half Ratio = Perimeter 1 (Small Half) / Perimeter 2 (Large Half)
Cell Half Ratio (Short Perimeter/Long Perimeter)
D
Pom1-mEGFP
wild type
sds23Δ
E
Cdr2-mEGFP
cdc25-degron-DAmP
sds23Δ
Cdr2-mEGFP FWHM (μm)
F
Mid1-13myc
untagged
wild type
sds23Δ
150-
α-myc
25-
α-cdc2
Normalized Band Intensity (a.u.)
G
Rlc1-mNeonGreen Sad1-mEGFP
-5 0 5 10 15 20 25 30 35 40 45 (min)
wild type
sds23Δ
H
wild type (n=15 cells)
sds23Δ (n=10 cells)
Fluorescence Intensity at CR (a.u.)
Time (min since SPB separation)

**Figure S1**

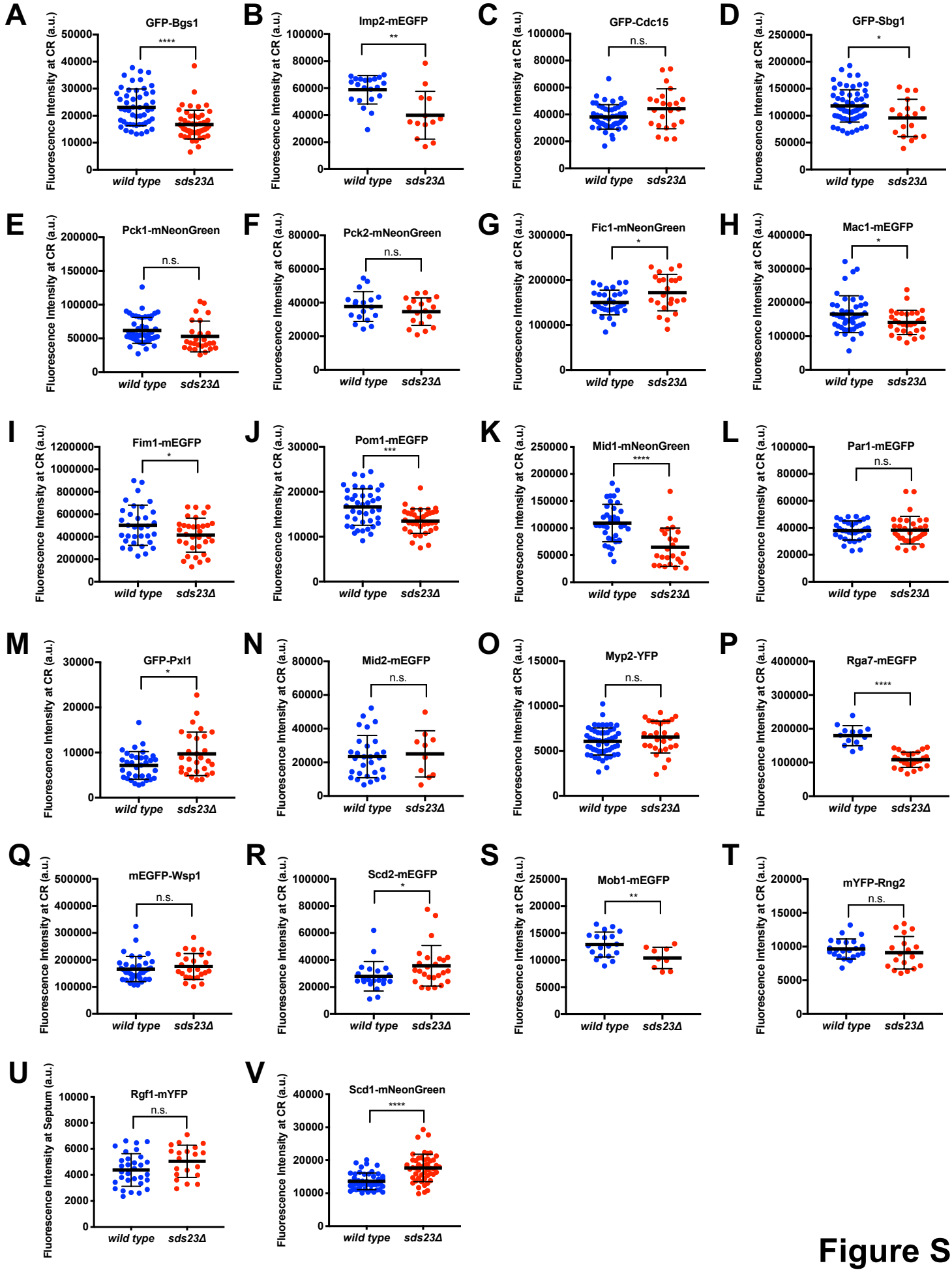
A
GFP-Bgs1
Fluorescence Intensity at CR (a.u.)
****
wild type
sds23Δ
B
Imp2-mEGFP
**
C
GFP-Cdc15
n.s.
D
GFP-Sbg1
*
E
Pck1-mNeonGreen
F
Pck2-mNeonGreen
G
Fic1-mNeonGreen
H
Mac1-mEGFP
I
Fim1-mEGFP
J
Pom1-mEGFP
***
K
Mid1-mNeonGreen
L
Par1-mEGFP
M
GFP-Pxl1
N
Mid2-mEGFP
O
Myp2-YFP
P
Rga7-mEGFP
Q
mEGFP-Wsp1
R
Scd2-mEGFP
S
Mob1-mEGFP
T
mYFP-Rng2
U
Rgf1-mYFP
Fluorescence Intensity at Septum (a.u.)
V
Scd1-mNeonGreen

**Figure S2**

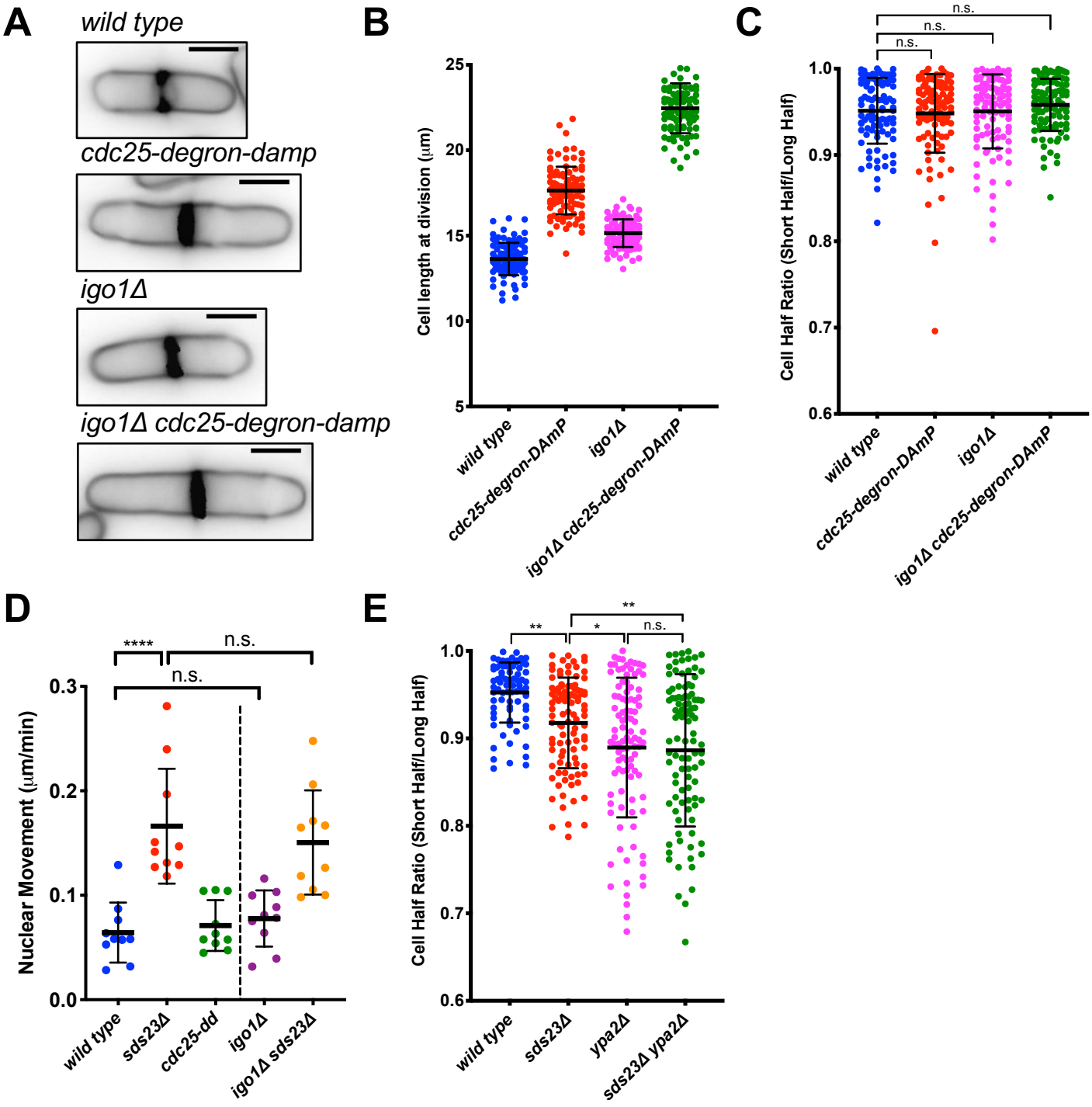
A
wild type
cdc25-degron-damp
igo1Δ
igo1Δ cdc25-degron-damp
B
Cell length at division (μm)
25
20
15
10
5
wild type
cdc25-degron-DAmP
igo1Δ
igo1Δ cdc25-degron-DAmP
C
Cell Half Ratio (Short Half/Long Half)
1.0
0.9
0.8
0.7
0.6
n.s.
n.s.
n.s.
wild type
cdc25-degron-DAmP
igo1Δ
igo1Δ cdc25-degron-DAmP
D
Nuclear Movement (μm/min)
0.3
0.2
0.1
0.0
****
n.s.
n.s.
wild type
sds23Δ
cdc25-dd
igo1Δ
igo1Δ sds23Δ
E
Cell Half Ratio (Short Half/Long Half)
1.0
0.9
0.8
0.7
0.6
**
**
*
n.s.
wild type
sds23Δ
ypa2Δ
sds23Δ ypa2Δ

**Figure S3**